Turbulence Characteristics of Switchback and Nonswitchback Intervals Observed by Parker Solar Probe

Sofiane Bourouaine[1,2] , Jean C. Perez[1] , Kristopher G. Klein[3] , Christopher H. K. Chen[4] , Mihailo Martinović[3] , Stuart D. Bale[4,5,6,7] , Justin C. Kasper[8] , and Nour E. Raouafi[2]

[1] Department of Aerospace, Physics and Space Sciences, Florida Institute of Technology, 150 West University Boulevard, Melbourne, Fl 32901, USA
sofiane.bourouaine@jhuapl.edu
[2] Johns Hopkins University, Applied Physics Laboratory, Laurel, MD 20723, USA
[3] Lunar and Planetary Laboratory, University of Arizona, Tucson, AZ 85719, USA
[4] School of Physics and Astronomy, Queen Mary University of London, London E1 4NS, UK
[5] Space Sciences Laboratory, University of California, Berkeley, CA 94720, USA
[6] Physics Department, University of California, Berkeley, CA 94720-7300, USA
[7] The Blackett Laboratory, Imperial College London, London SW7 2AZ, UK
[8] Department of Climate and Space Sciences and Engineering, University of Michigan, Ann Arbor, MI 48109, USA
Received 2020 July 15; revised 2020 September 29; accepted 2020 September 30; published 2020 December 2

Abstract

We use Parker Solar Probe (PSP) in situ measurements to analyze the characteristics of solar wind turbulence during the first solar encounter covering radial distances between $35.7R_\odot$ and $41.7R_\odot$. In our analysis we isolate so-called switchback (SB) intervals (folded magnetic field lines) from nonswitchback (NSB) intervals, which mainly follow the Parker spiral field. Using a technique based on conditioned correlation functions, we estimate the power spectra of Elsasser, magnetic, and bulk velocity fields separately in the SB and NSB intervals. In comparing the turbulent energy spectra of the two types of intervals, we find the following characteristics: (1) The decorrelation length of the backward-propagating Elsasser field z^- is larger in the NSB intervals than the one in the SB intervals; (2) the magnetic power spectrum in SB intervals is steeper, with spectral index close to $-5/3$, than in NSB intervals, which have a spectral index close to $-3/2$; (3) both SB and NSB turbulence are imbalanced with NSB having the largest cross-helicity, (4) the residual energy is larger in the SB intervals than in NSB, and (5) the analyzed fluctuations are dominated by Alfvénic fluctuations that are propagating in the sunward (antisunward) direction for the SB (NSB) turbulence. These observed features provide further evidence that the switchbacks observed by PSP are associated with folded magnetic field lines giving insight into their turbulence nature.

Unified Astronomy Thesaurus concepts: Solar wind (1534); Interplanetary turbulence (830); Magnetohydrodynamics (1964); Space plasmas (1544); Alfven waves (23); Plasma physics (2089); Heliosphere (711)

1. Introduction

Near-Sun solar wind observations by the Parker Solar Probe (PSP) during the first perihelion passes have revealed the frequent presence of the so-called magnetic *switchbacks* (SBs), which refer to local reversals of the radial magnetic field (Bale et al. 2019; Kasper et al. 2019; Dudok de Wit et al. 2020; Horbury et al. 2020; McManus et al. 2020). These switchbacks are usually associated with correlated enhancements of the radial plasma flow. The origin of these field reversals is still under investigation and it is unclear whether they arise from impulsive events in the lower corona (Roberts et al. 2018; Tenerani et al. 2020) or they form in situ due to, for example, Alfvénic turbulence in the expanding wind (Squire et al. 2020).

SBs have been previously observed in fast solar-wind streams near 0.3 au (Horbury et al. 2018) and near or beyond 1 au (Kahler et al. 1996; Balogh et al. 1999). However, the SBs observed recently by PSP during its first perihelion are detected in slow solar wind, and they are sharper and ubiquitous. These observed slow solar-wind streams are identified as originating from an equatorial coronal hole and are dominated by Alfvénic fluctuations (Bale et al. 2019; Kasper et al. 2019). The correlation between the speed enhancement and the presence of field reversals has been studied using Ulysses (beyond 1 au; Matteini et al. 2014). This correlation is interpreted as a result of a geometrical effect of the propagating large-scale Alfvénic fluctuations.

One interesting feature that characterizes the electron plasma in SB intervals as observed recently using the Solar Probe Analyzers SPAN-e instrument (Whittlesey et al. 2020) on PSP is that the electron strahl pitch angle distributions follow the magnetic field through SBs (Kasper et al. 2019). Ulysses measurements also show that the relative proton beam appears to move slower than the proton core (in the spacecraft frame) following the reversed local field (Neugebauer & Goldstein 2013). Furthermore, Yamauchi et al. (2004) showed that if the magnetic field is folded back on itself, alpha particles will locally have radial flow speeds less than protons. The relative motion of protons and alphas during switchback periods near 0.3 au has also been discussed in Matteini et al. (2015). A more recent study of proton core-beam reversals with PSP data shows that the proton core parallel temperature is the same inside and outside of switchbacks (Woolley et al. 2020), indicating more evidence that Alfvénic pulses travel along open magnetic field lines.

Another important observed feature of SBs is that turbulence is dominated by sunward-propagating Alfvénic fluctuations over antisunward ones, an indication that Alfvénic fluctuations propagating away from the Sun are following folded magnetic field lines. This feature has been observed near the Sun at

0.16 au using PSP (McManus et al. 2020), and also at heliocentric distances larger than 1 au using Ulysses (Balogh et al. 1999).

In this paper we investigate turbulence characteristics in the SB and nonswitchback (NSB) regions using a technique based on conditioned correlation functions. In Section 2 we present our data analysis and methodology to identify SB and NSB time intervals. In Section 3 we estimate the correlation functions, the power spectra, the normalized cross-helicity, and the residual energy corresponding to those time intervals. Finally, in Section 4 we conclude and discuss our results.

2. Data and Methodology

In our analysis we investigate the SBs that were observed during the first encounter (E1) between 2018 November 3 and 9. During this time period PSP observed heliocentric distances ranging from 35.7 $R_\odot$ to about 41.7 $R_\odot$ (Fox et al. 2016). We use combined plasma and magnetic field measurements in the level-three data from SWEAP and level-two data from FIELDS on board PSP, respectively. Data were obtained from the Solar Probe Cup (SPC; Case et al. 2020) and the FIELDS flux-gate magnetometer (MAG; Bale et al. 2016). During this period, the data were measured with a time resolution of about 0.874 s for plasma moments and 0.22 s for the magnetic field vector. In our study we fit plasma and averaged magnetic field data to a uniform time grid with the resolution of the plasma data (i.e., 0.874 s). We also use a time-domain Hampel filter to remove artificial spikes within the plasma data (Liu et al. 2004).

Figure 1(a) shows the three components of the magnetic field vector in the RTN coordinate system (where R is the direction from the Sun's center to the spacecraft, T is the tangential component that results from the cross-product of the solar rotation vector with R, and N is the normal component that completes the right-handed system). The B_R component frequently flips from the sunward to the antisunward direction during some time intervals. Overall, the magnetic field is strongly deflected from the expected Parker field line with large angles. For a detailed description of these time signals, see Dudok de Wit et al. (2020).

In this paper we isolate the intervals that correspond to SBs (NSBs) within regions where $B_R > 0$ ($B_R < 0$). Before we isolate the SB and the NSB intervals we first estimate the decorrelation times $\tau_{c,out}$ and $\tau_{c,in}$ of magnetic field fluctuations in regions where the magnetic field radial component points outward (from the Sun) $B_R > 0$ and inward $B_R < 0$, respectively. We estimate those decorrelation times for the magnetic field using the following conditioned correlation functions,

$$C_{out}(\tau) \equiv \langle (\boldsymbol{B}(t) - \overline{\boldsymbol{B}}) \cdot (\boldsymbol{B}(t + \tau) - \overline{\boldsymbol{B}}) \rangle_{B_R > 0}, \quad (1)$$

$$C_{in}(\tau) \equiv \langle (\boldsymbol{B}(t) - \overline{\boldsymbol{B}}) \cdot (\boldsymbol{B}(t + \tau) - \overline{\boldsymbol{B}}) \rangle_{B_R < 0}, \quad (2)$$

where the symbols $\langle \cdots \rangle_{B_R > 0}$ and $\langle \cdots \rangle_{B_R < 0}$ denote the ensemble average, which can be computed over many realizations (or averaged over time t) conditioned by $B_R > 0$ or $B_R < 0$. Here $\overline{\boldsymbol{B}}$ are obtained by averaging over the same ensemble, i.e., all those points used in the calculation of the correlation functions. The time lag τ is varied from 0 to 1.5 hr.

Figure 1(b) displays the normalized correlation functions $\Gamma_{out}(\tau) \equiv C_{out}(\tau)/C_{out}(0)$ (solid line) and $\Gamma_{in}(\tau) \equiv C_{in}(\tau)/C_{in}(0)$ (dotted line) as a function of τ. We find that the magnetic decorrelation times are $\tau_{c,out} \simeq 2$ minutes and
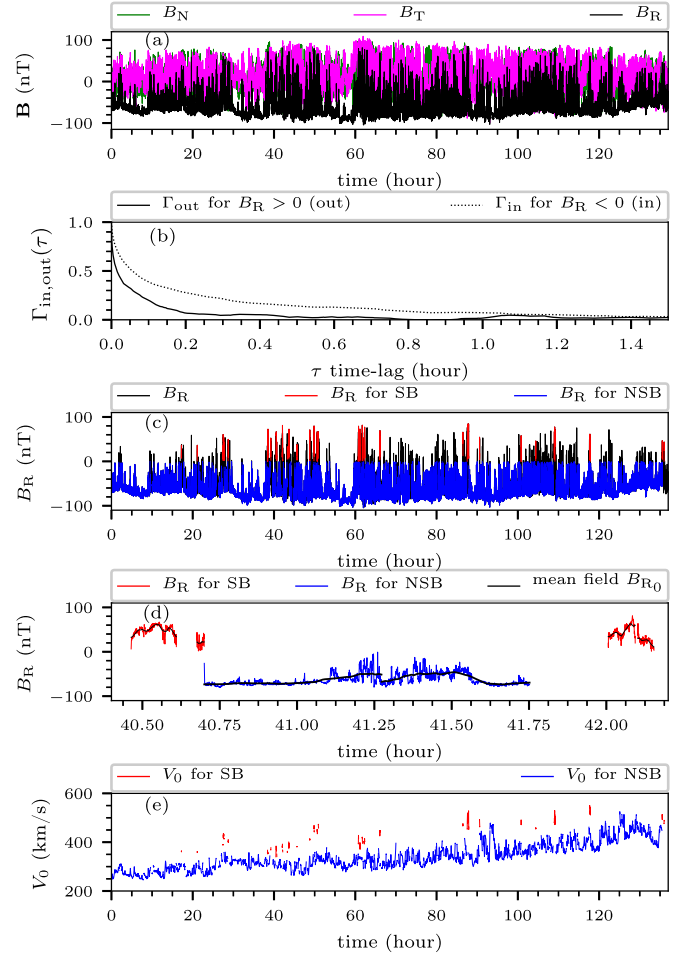

Figure 1. Panels from top to bottom correspond to PSP observations from 2018 November 3 to 9. (a) Time signal for magnetic field vector in RTN coordinates. (b) The normalized correlation of the magnetic field conditioned with $B_R > 0$ and $B_R < 0$ plotted vs. time lag τ. (c) The radial component B_R that belongs to the selected to SB intervals (red), NSB intervals (blue), and nonselected intervals (black). (d) For clarity we plot a subset of isolated SB (red) and NSB (blue) intervals within a 2 hour long subinterval, and (e) the mean velocity V_0 for SB (red) and NSB (blue) intervals.

$\tau_{c,in} \simeq 6$ minutes (times for which $\Gamma_{out,in} = 1/e$), meaning that the magnetic turbulent fluctuations in strongly reversed field decorrelate faster in time. Note that the obtained decorrelation time $\tau_{c,in} \simeq 6$ minutes is within the variation range of the magnetic decorrelation time found by Chen et al. (2020), Parashar et al. (2020).

We next identify the SB (NSB) intervals inside the $B_R > 0$ ($B_R < 0$) regions. One criterion we use to isolate the SB and NSB intervals is to consider continuous measurements of $B_R > 0$ ($B_R < 0$) that last at least a period of time $T \gtrsim \tau_{c,out}$ ($\tau_{c,in}$) for SB (NSB) intervals. In this way we designate SB and NSB time intervals with time lengths equal to or higher than the corresponding magnetic decorrelation time periods, allowing for a proper estimation of the correlated fluctuations and their associated local mean field.

In Figure 1(c) we plot the radial component B_R associated with the SB (red) and NSB (blue) time intervals. The intervals with black colors are those intervals that do not satisfy the criteria described above. Figure 1(d) shows the SB and NSB intervals within a 2 hour subinterval to illustrate this selection process.
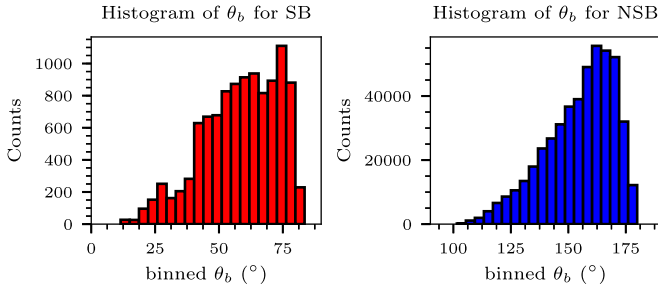
Figure 2. Histograms illustrating the number of points that correspond to the angle θ_b in the SB (left panel) and NSB (right panel) intervals.

We use the obtained decorrelation times, $\tau_{c,out}$ and $\tau_{c,in}$ to define the local mean magnetic field within the SB and NSB intervals as

$$\boldsymbol{B}_0(t_j) = \frac{1}{N_j} \sum_i W_T(t_j - t_i) \boldsymbol{B}(t_i), \qquad (3)$$

where N_j is the number of averaging samples and $W_T(t)$ is a windowing function that vanishes everywhere except for $|t| \leqslant T/2$, where it is equal to one. The period T is chosen to be equal to the decorrelation time such that $T = \tau_{c,out}$ (for SBs) or $T = \tau_{c,in}$ (for NSBs). The radial component B_{0R} is plotted in black in Figure 1(d). The mean velocity $\boldsymbol{V}_0$ can be estimated in a similar fashion by replacing $\boldsymbol{B}$ with $\boldsymbol{V}$ in Equation (3). Figure 1(e) displays the mean speed V_0 for the SB (red) and NSB (blue) intervals. The figure shows that the mean velocity profiles for SB and NSB have an increasing trend from values 340 to 550 km s^{-1} for SB and from 245 to 520 km s^{-1} for NSB. The percentage increase of the mean velocity in the NSB intervals is about a 100% versus a 60% increase in SB intervals.

Determining the local mean magnetic field allows for the estimation of the local angle $\theta_b \equiv (\hat{\boldsymbol{R}}, \boldsymbol{B}_0)$ between the radial direction $\hat{\boldsymbol{R}}$ and the local magnetic field.

Figure 2 displays the histogram for the occurrence of the angle θ_b for SB configurations (left panel) and NSB configurations (right panel). As expected, the most common angle θ_b for NSB intervals is $\theta_b \simeq 170°$, which is close to the Parker field angle. The angle θ_b varies from 100° to 175° in the NSB intervals, and from about 10° to 80° in the SB intervals. The most likely angles θ_b in SB intervals range between 40° and 75°.

It is worth mentioning that the outcomes from the analysis below are not sensitive to the choice of θ_b range for SB and NSB intervals. For example, we repeated the analysis considering a narrow range of θ_b with $\theta_b > 150°$ characterizing NSB intervals and a wide range of θ_b with $\theta_b < 150°$ characterizing SB intervals, and the obtained results were comparable to the ones that we report in this work.

3. Turbulence Characteristics in SB and NSB Intervals

We use a technique based on so-called conditioned correlation functions (described in Bourouaine & Perez 2020) to estimate the power spectra from discontinuous intervals. The power spectra that correspond to Elsasser fields $z^{\pm}$, velocity field $\boldsymbol{V}$, and magnetic field $\boldsymbol{B}$ from these discontinuous SB and NSB intervals can then be derived from their corresponding conditioned correlation functions. Here, the Elsasser fields are

defined as $\boldsymbol{z}^{\pm} = \boldsymbol{V} \pm \boldsymbol{V}_A$, where $\boldsymbol{V}_A = \boldsymbol{B}\big/\sqrt{4\pi\rho}$ is the Alfvén velocity where ρ is the proton mass density.

In this technique we treat these discontinuous intervals as statistical realizations to estimate various correlation functions and simply create ensembles in which the fields have certain properties (conditioning) under an implicit underlying assumption, which is that ergodicity applies to these ensembles. The Fourier transform of these correlation functions can be used to determine the corresponding power spectra. Let us first define the conditioned correlation functions of the various fields for SB and NSB as follows

$$C_q^{SB}(\tau) = \langle (\boldsymbol{q}(t) - \overline{\boldsymbol{q}}) \cdot (\boldsymbol{q}(t + \tau) - \overline{\boldsymbol{q}}) \rangle_{SB, V_0}, \qquad (4)$$

$$C_q^{NSB}(\tau) = \langle (\boldsymbol{q}(t) - \overline{\boldsymbol{q}}) \cdot (\boldsymbol{q}(t + \tau) - \overline{\boldsymbol{q}}) \rangle_{NSB, V_0}, \qquad (5)$$

where the generic vector $\boldsymbol{q}$ can represent the Elsasser variables $\boldsymbol{z}^{\pm}$, the velocity $\boldsymbol{V}$, or magnetic $\boldsymbol{B}$ fields. The correlation functions are computed over many realizations (or averaged over time t) conditioned by SB or NSB selected intervals (defined above) and the solar wind speed V_0. Here, we condition the correlations by considering only the statistics of those two times t and $t + \tau$ in Equations (4) and (5) that belong to SB and NSB intervals, respectively. In order to ensure that we are dealing with the same stream or turbulence we do not allow for a significant variation in the mean solar-wind velocity. Therefore we condition the correlation functions with respect to mean velocity V_0 and consider only those points where their corresponding values of V_0 vary from a minimum value $V_{0,min}$ corresponding to SB or NSB intervals to a maximum value $V_{0,max} \simeq 1.5 \times V_{0,min}$ (a 50% increase).

There are three main advantages of calculating the power spectra through the correlation functions: (1) one can deal with discontinuous intervals (such as the SB and NSB intervals for our case) and avoid any unwanted points, including gaps of bad measurements in the calculation of the correlation functions, (2) one can obtain the correlation functions at time lags (including correlation times) much longer than the periods of the used discontinuous intervals, and (3) one can check the statistics that correspond to the estimation of the correlation functions for each time lag τ. In addition, further conditioning the correlation functions, for example, with respect to solar wind velocity, ensures that discontinuous intervals are associated with a single stream (or single kind of turbulence). In many cases, using the standard method of estimating the power spectra through the Fourier transform of continuous time signals does not guarantee one can avoid mixing measurements from qualitatively different streams, such as when the spacecraft is crossing solar wind streams with a significant difference in speed. Such continuous time signals mixing different speeds may artificially increase the kinetic energy of the outer scale.

Figures 3(a) and (b) show the normalized correlation functions $\Gamma_q^{SB}(\tau) \equiv C_q^{SB}(\tau)\big/C_q^{SB}(0)$ and $\Gamma_q^{NSB}(\tau) \equiv C_q^{NSB}(\tau)\big/C_q^{NSB}(0)$ computed using Equations (4) and (5), respectively. Interestingly enough, the curves of the normalized correlation functions that correspond to SB intervals drop relatively faster than those ones corresponding to NSB intervals. For NSB intervals, the largest decorrelation time corresponds to the Elsasser field z^-, which is about $\simeq 3$ hr, then after, the velocity decorrelation time is about $\simeq 9$ minutes. Also, the decorrelation times corresponding to Elsasser field z^+ and magnetic field $\boldsymbol{B}$ are identical and close to 6 minutes in the
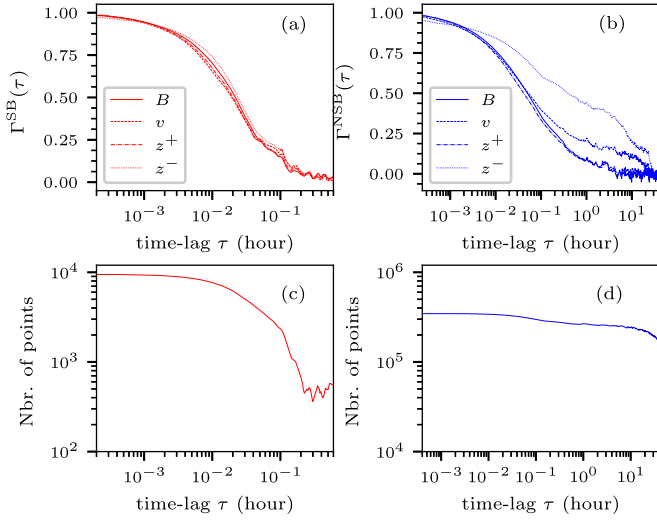
Figure 3. Upper panels: the normalized correlation function for the variables q using for SB intervals (panel (a)) and for NSB intervals (panel (b)). All plotted vs. time-lag τ. Lower panels: the number of points that correspond to the calculation of the correlation function for the SB (panel (c)) and NSB (panel (d)) intervals. The SB correlation functions drop to zero at a time lag that is much smaller than 0.6 hr, and there is no need to extend the time-lag to values bigger than 0.6 hr where the number of statistical points starts to decrease.

Figure 4. Left panels: spacecraft-frame power spectra of v, b, and $z^{\pm}$ for SB intervals. Right panels: spacecraft-frame power spectra v, b, and $z^{\pm}$ for NSB intervals. All spectra are plotted vs. frequency f. Power-law fits with spectral index (colored dashed–dotted lines) are added. The magnetic power spectra were multiplied by a factor of 10 for easy viewing. The vertical dotted line was plotted to refer to the noise level in the power spectra for v and z^-. All the power spectra were multiplied by a factor of 2 to account for their negative frequency part. The uncertainty on z^- power spectra were plotted with dashed magenta lines.

NSB intervals. However, for SB intervals, the decorrelation times corresponding to all fields q seem to be identical and close to 2 minutes.

To estimate the corresponding perpendicular correlation lengths from the obtained correlation times we invoke Taylor's Hypothesis. Although the ratio $V_A/V_\perp \sim 1$ (where $V_\perp$ is the perpendicular velocity of the spacecraft seen in the plasma frame), Bourouaine & Perez (2019, 2020), Perez & Bourouaine (2020) showed that Taylor approximation can still be valid if the dimensionless parameter $\epsilon = \delta u_0/(\sqrt{2}\,V_\perp) \lesssim 0.5$ (where δu_0 is the outer-scale fluid velocity) and under the assumption that the turbulence is strong. Here we found that $\epsilon \simeq 0.15 \pm 0.02$ ($\epsilon \simeq 0.30 \pm 0.08$) for SB (NSB) intervals. $V_\perp$ is estimated by taking into account the spacecraft velocity, $V_{sc} = 92$ km s^{-1}, which is tangential. The errors in ϵ are estimated due to error in velocity fluctuation caused by the noise and the uncertainty in the bulk velocity. The correlation lengths can be obtained through the decorrelation time t_c as $\lambda_c \simeq V_\perp t_c$, where $V_\perp = 253$ km s^{-1} ($V_\perp = 119$ km s^{-1}) for SB (NSB) intervals. This leads to correlation lengths $\lambda_c \simeq 30,000$ km for B, $z^{\pm}$ and V fields in SB intervals. In NSB intervals, the correlations length of B and z^+ is $\lambda_c \simeq 35,000$ km, which is comparable to the one in SB intervals, and the correlation lengths corresponding to V and z^- fields are about 64,000 km and 1 Mm, respectively.

Figures 3(c)–(d) show the number of points used in the calculations of the correlation functions in SB (lower left) and NSB (lower right) intervals. As expected, we have a smaller sample size for SB intervals. However, these correlation functions were still computed with sufficient statistics for time lags up to 0.6 hr $\tau \leqslant 0.6$ hr, which is much higher than the correlation times in the SB intervals.

In Figure 4 we plot the power spectra of all variables q, which were computed as the Fourier transform of their corresponding correlation functions (plotted in Figure 3)

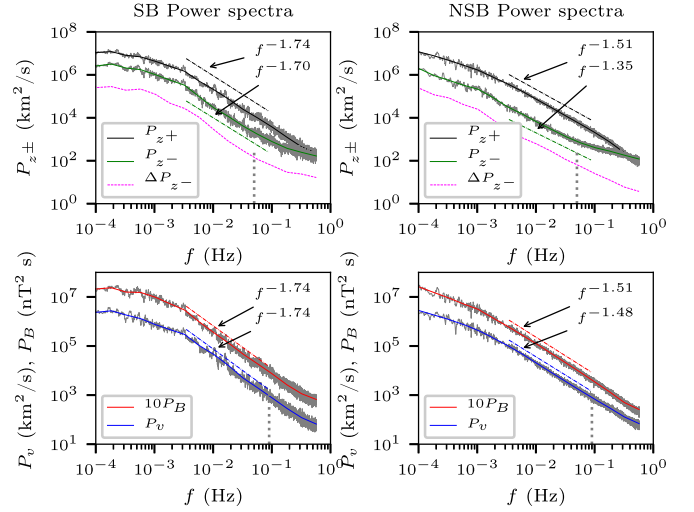$$P_q(f) \equiv \frac{1}{2\pi} \int_{-\infty}^{\infty} C_q(\tau)e^{i2\pi f\tau}d\tau. \tag{6}$$

The power spectra corresponding to SB (left panel) and NSB (right panel) intervals are plotted versus the frequency f in the spacecraft frame. These power spectra were computed using correlation functions that span over time lags that are much larger than the decorrelation times.

Our analysis shows that the energy of fluctuations in the SB intervals follows a power-law turbulent spectrum, indicating that a broad turbulence spectrum of fluctuations occurs within SB intervals. Furthermore, it seems that the power spectra in SB intervals are relatively steeper following a power law with spectral index of about -1.7 (close to $-5/3$) for all variables, whereas in the NSB intervals the power spectra corresponding to B, z^+, and v follow a power-law with spectral index that is close to $-3/2$. However, the power spectrum corresponding to z^- in NSB follow a power law with a spectral index -1.35. The noise levels in the velocity and the z^- power spectra are shown using two vertical dotted lines in Figure 4. The noise level starts to occur at frequencies higher than $f \simeq 10^{-1}$ Hz in the velocity spectra, and higher than $\simeq 5 \times 10^{-2}$ Hz in the z^- spectra. The estimation of the noise level were based on the high-frequency flattening observed in the velocity power spectrum calculated from continuous and evenly spaced 7 hour long time interval on 2018 November 6. In this time interval only a few interpolations were applied due to some missing points. The observed flattening in the v power spectrum occurs at frequency $f \simeq 10^{-1}$ Hz that is consistent with one found in Chen et al. (2020).

To rule out that the measured minor z^- spectra are not spurious due to measurement uncertainties, we estimate their corresponding uncertainties for SB and NSB intervals in Figure 5 (magenta dashed lines) based on the uncertainties on velocity components and density. We used the upper estimate of the uncertainty on the moments due to, for example, the amount of background noise in the current spectra, alpha-proton VDF separation, etc., provided in the SPC L3I data. The averaged relative uncertainties on the velocity components are
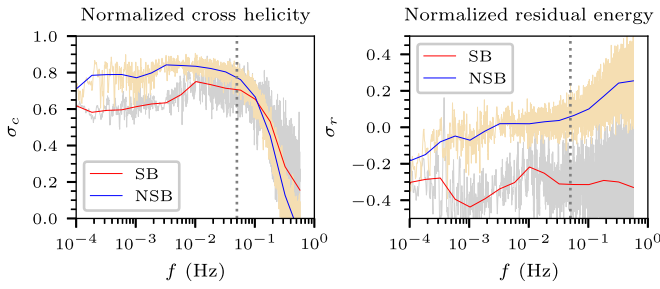
Figure 5. Left panel: normalized cross-helicity for SB (red) and NSB (blue). Right panel: normalized residual energy for SB (red) and NSB (blue). All plotted as a function of the frequency f. The curves at frequencies higher than 5×10^{-2} Hz (vertical dotted line) may be contaminated by the noise.

about 5% for the radial component and about 20% for the other components, and the relative uncertainty of the density is about 20%. The relative uncertainty on the z^- power spectrum is found to be about 10%, which indicates that the measured z-spectrum is physical and not spurious.

In Figure 5 we plot the normalized cross-helicity from the Elsasser fields as $\sigma_c = (P_{z^+} - P_{z^-})/(P_{z^+} + P_{z^-})$ (where $P_{z^\pm}$ is the power spectra corresponding to $z^\pm$) and the normalized residual energy $\sigma_r = (P_v - P_B)/(P_v + P_B)$ (where P_v and P_B are the power spectra corresponding to v and $\mathbf{B}$) for the SB (red) and NSB (blue) turbulence. The noise may affect the curves of σ_r and σ_c at frequencies higher than 5×10^{-2} Hz, and therefore we exclude this frequency range from any physical interpretation.

Here we notice that the normalized cross-helicity of the turbulent field is positive for both SB and NSB intervals. The turbulence is then dominated by the z^+ fluctuations, which means that the Alfvén fluctuations propagate antisunward in the NSBs and in the sunward direction in the SBs. Furthermore, we found that the turbulence is more imbalanced in the NSB intervals than in the SB intervals.

It is worth noting that the magnitude of the normalized residual energy in the SB turbulence is higher than the one corresponding to NSB turbulence. Also, steepness in the magnetic power spectrum in the SB intervals may be due to the fact that $|\sigma_r|$ for the SB turbulence is higher than $|\sigma_r|$ for the NSB turbulence. The connection between the steepness of the magnetic spectrum and the normalized residual energy was studied in a number of previous works near 1 au (see, for instance, Boldyrev et al. 2011). The finding of the magnetic field and total energy spectra becoming steeper as the turbulence becomes more balanced is consistent with 1 au observations (Chen et al. 2013).

4. Discussion and Conclusion

In this work we have used a methodology based on conditioned correlation functions to analyze the characteristics of the turbulence in the SB and NSB intervals at heliocentric distances from $35.7R_\odot$ to $41.7R_\odot$. The power spectra that correspond to Elsasser fields as well as the velocity and magnetic fields were then computed as the Fourier transform of these conditioned correlations functions. We found that the correlation lengths of the variables B and z^+ in SB and NSB intervals are comparable. However, the estimated correlation length of z^- in NSB intervals is about 1 Mm and it is much larger that the one (about 30,000 km) in the SB intervals. The long correlation lengths (or correlation times) of z^- within the

NSB intervals are similar to those found by Chen et al. (2020), which was interpreted as consistent with the generation of z^- fluctuations from non-WKB (Wentzel-Kramers-Brillouin) reflections of z^+ due to inhomogeneity of the background plasma along the magnetic field line (Heinemann & Olbert 1980; Hollweg 1981; Velli 1993; Hollweg & Isenberg 2007; Chandran & Hollweg 2009; Verdini et al. 2012; Perez & Chandran 2013; Chandran & Perez 2019). The new finding here is that in the SB intervals the correlation time is shorter and the same in all fields, illustrating the different nature of the fluctuations within the switchbacks. Here, we conjecture that because non-WKB reflections occur more efficiently for AW fluctuations with long parallel wavelengths, of the order of one solar wind radius (as our estimates indicate in the NSB; Perez & Chandran 2013; Chandran & Perez 2019), long-wavelength correlated fluctuations arising from reflections are suppressed within the SBs, as SBs are likely to be much smaller.

Furthermore, we found that turbulence in SBs is more balanced than in NSBs, and the magnetic power spectrum corresponding to SB turbulence is steeper than that corresponding to NSB turbulence. This observed steepening in the power spectra with more balanced turbulence is also associated with a larger amount of residual energy. This finding seems to be consistent with previous 1 au measurements (Chen et al. 2013; Bowen et al. 2018). Moreover, one possibility for why the turbulence is more balanced in SB intervals is that it is locally driven, either by velocity shear introduced by the SBs or by the oppositely directed waves on neighboring field lines that are traveling in both directions due to the folded field. Therefore, the analysis presented here contributes to a better understanding of the nature of the switchback turbulence and may provide empirical insights on the process of reflection-driven turbulence inside and outside switchbacks.

ORCID iDs

Sofiane Bourouaine ⓘ https://orcid.org/0000-0002-2358-6628
Jean C. Perez ⓘ https://orcid.org/0000-0002-8841-6443
Kristopher G. Klein ⓘ https://orcid.org/0000-0001-6038-1923
Christopher H. K. Chen ⓘ https://orcid.org/0000-0003-4529-3620
Mihailo Martinović ⓘ https://orcid.org/0000-0002-7365-0472
Stuart D. Bale ⓘ https://orcid.org/0000-0002-1989-3596
Justin C. Kasper ⓘ https://orcid.org/0000-0002-7077-930X
Nour E. Raouafi ⓘ https://orcid.org/0000-0003-2409-3742

References

Bale, S. D., Badman, S. T., Bonnell, J. W., et al. 2019, Natur, 576, 237
Bale, S. D., Goetz, K., Harvey, P. R., et al. 2016, SSRv, 204, 49
Balogh, A., Forsyth, R. J., Lucek, E. A., Horbury, T. S., & Smith, E. J. 1999, GeoRL, 26, 631

Boldyrev, S., Perez, J. C., Borovsky, J. E., & Podesta, J. J. 2011, ApJL, 741, L19
Bourouaine, S., & Perez, J. C. 2019, ApJL, 879, L16
Bourouaine, S., & Perez, J. C. 2020, ApJL, 893, L32
Bowen, T. A., Mallet, A., Bonnell, J. W., & Bale, S. D. 2018, ApJ, 865, 45
Case, A. W., Kasper, J. C., Stevens, M. L., et al. 2020, ApJS, 246, 43
Chandran, B. D. G., & Hollweg, J. V. 2009, ApJ, 707, 1659
Chandran, B. D. G., & Perez, J. C. 2019, JPlPh, 85, 905850409
Chen, C. H. K., Bale, S. D., Bonnell, J. W., et al. 2020, ApJS, 246, 53
Chen, C. H. K., Bale, S. D., Salem, C. S., & Maruca, B. A. 2013, ApJ, 770, 125
Dudok de Wit, T., Krasnoselskikh, V. V., Bale, S. D., et al. 2020, ApJS, 246, 39
Fox, N. J., Velli, M. C., Bale, S. D., et al. 2016, SSRv, 204, 7
Heinemann, M., & Olbert, S. 1980, JGR, 85, 1311
Hollweg, J. V. 1981, SoPh, 70, 25
Hollweg, J. V., & Isenberg, P. A. 2007, JGRA, 112, A08102
Horbury, T. S., Matteini, L., & Stansby, D. 2018, MNRAS, 478, 1980
Horbury, T. S., Woolley, T., Laker, R., et al. 2020, ApJS, 246, 45
Kahler, S. W., Crooker, N. U., & Gosling, J. T. 1996, JGR, 101, 24373
Kasper, J. C., Bale, S. D., Belcher, J. W., et al. 2019, Natur, 576, 228
Liu, H., Shah, S., & Jiang, W. 2004, Computers Chemical Engineering, 28, 1635
Matteini, L., Horbury, T. S., Neugebauer, M., & Goldstein, B. E. 2014, GeoRL, 41, 259
Matteini, L., Horbury, T. S., Pantellini, F., Velli, M., & Schwartz, S. J. 2015, ApJ, 802, 11
McManus, M. D., Bowen, T. A., Mallet, A., et al. 2020, ApJS, 246, 67
Neugebauer, M., & Goldstein, B. E. 2013, in AIP Conf. Ser. 1539, Solar Wind 13, ed. G. P. Zank et al. (Melville, NY: AIP), 46
Parashar, T. N., Goldstein, M. L., Maruca, B. A., et al. 2020, ApJS, 246, 58
Perez, J. C., & Bourouaine, S. 2020, PhRvR, 2, 023357
Perez, J. C., & Chandran, B. D. G. 2013, ApJ, 776, 124
Roberts, M. A., Uritsky, V. M., DeVore, C. R., & Karpen, J. T. 2018, ApJ, 866, 14
Squire, J., Chandran, B. D. G., & Meyrand, R. 2020, ApJL, 891, L2
Tenerani, A., Velli, M., Matteini, L., et al. 2020, ApJS, 246, 32
Velli, M. 1993, A&A, 270, 304
Verdini, A., Grappin, R., Pinto, R., & Velli, M. 2012, ApJL, 750, L33
Whittlesey, P. L., Larson, D. E., Kasper, J. C., et al. 2020, ApJS, 246, 74
Woolley, T., Matteini, L., Horbury, T. S., et al. 2020, arXiv:2007.10906
Yamauchi, Y., Suess, S. T., Steinberg, J. T., & Sakurai, T. 2004, JGRA, 109, A03104